Arabian Journal of Geosciences (2019) 12: 299
https://doi.org/10.1007/s12517-019-4459-0

ORIGINAL PAPER

Ore genesis of the Baiyun gold deposit in Liaoning province, NE China: constraints from fluid inclusions and zircon U–Pb ages

Guotao Sun[1,2,3] · Qingdong Zeng[1,2,3] · Taiyang Li[4] · An Li[4] · Enyuan Wang[4] · Chunsheng Xiang[4] · Yongbin Wang[1,2] · Peiwen Chen[1,2,3] · Bing Yu[1,2,3]

Received: 12 October 2018 / Accepted: 1 April 2019 / Published online: 26 April 2019

Abstract

The Baiyun gold deposit in the Liaodong gold province, NE, North China Craton (NCC), is a lode gold deposit hosted within the Paleoproterozoic metamorphic rocks. Disseminated and vein-hosted gold mineralization occurs along NWW-trending interlayer faults and NE-trending normal faults. Crosscutting relationships and mineral assemblages indicate hydrothermal process of the gold deposit can be divided into three stages, characterized by pyrite–quartz (stage 1), quartz–pyrite–chalcopyrite (stage 2), and quartz–carbonate (stage 3) assemblages. Gold is observed within stage 1 and 2 veins. Hessite is observed within stage 2 veins. Fluid inclusion petrography and microthermometry indicate that the ore fluid evolved from moderate salinities to low salinities, likely due to fluid mixing. The precipitation of gold and hessite is attributed to fluid mixing. Fluid inclusion compositions present the minimum trapping temperatures of the ore fluid were between 200 and 290 °C. Minimum trapping pressures estimated from H_2O–CO_2–NaCl inclusions were 58–139 and 24–68 MPa for stage 1 and 2 assemblages, respectively. The $\delta^{18}O_{water}$ (‰ SMOW) values of ore fluid in stage 1 range from 3.9 to 7.8 ‰, and the δD (‰ SMOW) values are between − 92 and − 69‰, indicating that the ore fluid was dominantly magmatic water. Zircon from a pre-ore quartz porphyry yielded a weighted mean zircon $^{206}Pb/^{238}U$ age of 127.8 ± 0.8 Ma, and the emplacement of a post-ore microdiorite is constrained to 125.6 ± 1.3 Ma. These results suggest that the Baiyun gold deposit is an intrusion-related vein gold deposit formed at ~ 126 Ma, which coincides with extension and a peak in magmatism within the NCC, indicating that gold mineralization in this region might have resulted from the breakup of the NCC.

Keywords Fluid inclusion · Fluid mixing · Zircon U–Pb · Baiyun gold deposit · Eastern Liaoning province

Introduction

In the eastern North China Craton (NCC), lode gold deposits are observed within uplifted Precambrian basement. These deposits are characterized by quartz vein and altered rock (hydrothermal altered rock accompanied by addition of disseminated pyrite and gold without development of quartz veins) types, and are spatially associated with the Late Mesozoic intrusive bodies (Zhang et al. 2003; Fan et al. 2003; Li et al. 2013; Zhu et al. 2015; Yang et al. 2016; Groves and Santosh 2016). The Liaodong gold province in NE China contains mesothermal lode deposits, similar to the Jiaodong gold province which is the most important gold producer in China. Few studies have been conducted on lode gold deposits within the Liaodong province, and the source of gold, timing of gold deposition, mechanism of gold precipitation, and overall classification of the deposits remain unclear. The Baiyun gold deposit in the central region of the Liaodong gold province provides an

Editorial handling: Maurizio Barbieri

Electronic supplementary material The online version of this article (https://doi.org/10.1007/s12517-019-4459-0) contains supplementary material, which is available to authorized users.

✉ Qingdong Zeng
zengqingdong@mail.iggcas.ac.cn

[1] Key Laboratory of Mineral Resouces, Institute of Geology and Geophysics, Chinese Academy of Sciences, Beijing 100029, China

[2] Institutions of Earth Science, Chinese Academy of Sciences, Beijing 100029, China

[3] University of Chinese Academy of Sciences, Beijing 100049, China

[4] Liaoning Zhaojin Baiyun Gold Mining Corporation, Dandong 118107, China

opportunity to study the fluid history and timing of gold deposition in the area. Previous studies focused on geological features, the timing and mode of ore formation, and thought that the gold mineralization was related to the Triassic magmatism (Liu and Ai 2000; Liu et al. 2012a; Zhang et al. 2016; Zhou 2017). However, previous experimental data on ore fluids were rather rare (Liu and Ai 1999; Hao et al. 2017). This paper describes the characteristics of the Baiyun gold deposit, focusing on the pressure–temperature evolution of ore fluids and the timing of gold mineralization. We applied multiple microanalytical techniques, such as scanning electron microscopy–based backscattered electron (SEM–BSE) imaging, Raman spectroscopy, microthermometry, and laser ablation–inductively coupled plasma–mass spectrometry (LA–ICP–MS). Our data are used to characterize the physical and chemical evolution of the ore fluids and to constrain the timing of gold deposition.

Geological setting

Regional geology

The Liaodong gold province is located at the northeastern margin of the NCC (Fig. 1a). The region underwent deformation and metamorphism during the Proterozoic, and extensive deformation and magmatism in the Mesozoic (Wu et al. 2005b). Regional lithostratigraphy is dominated by the Precambrian metamorphic rocks (Fig. 1b). The Archean Anshan complex, which is a series of 3800–3000 Ma tonalite–trondhjemite–granodiorite (TTG) gneisses (the oldest in North China) associated with 2500 Ma granitoids and supracrustal rocks, crops out in the north of the study area (Liu et al. 1992, 2008; Song et al. 1996; Wang et al. 2015a). The Paleoproterozoic units in the region comprise the Liaohe Group and the Liaoji Granitoids, which were metamorphosed under greenschist- to lower-amphibolite-facies conditions at 1900 Ma (Luo et al. 2004; Lu et al. 2006; Xie et al. 2011; Meng et al. 2014; Wang et al. 2016, 2017). The NWW-trending Liaohe Group unconformably overlying Archean units is overlain by Neoproterozoic strata, and, from bottom to top, comprises the Langzishan, Dashiqiao, and Gaixian formations. Deposition of the Liaohe Group is constrained to 2200–1950 Ma by zircon U–Pb dating of sedimentary and volcanic rocks (Luo et al. 2004, 2008; Wan et al. 2006; Liu et al. 2012b; Hu et al. 2015). The Liaoji granitoids crop out over an area of 300 × 70 km^2 in the central and southern sections of the Liaoji belt, and were emplaced mainly during the period of 2200–2140 Ma (Luo et al. 2004; Lu et al. 2006). The region also contains ~ 20,000 km^2 of Phanerozoic intrusions that were emplaced primarily during the Mesozoic, especially the Jurassic and Cretaceous (Fig. 1b). Jurassic granites (180–153 Ma), comprising monzogranite and granodiorite, had undergone regional ductile deformation. In contrast, Cretaceous intrusions (131–117 Ma), which comprise diorite, granodiorite, monzogranite, syenogranite, and syenite, are typically undeformed and more widely distributed than the Jurassic granites (Wu et al. 2005a, b).

Gold deposits in the Liaodong gold province are concentrated in three orefields (the Qingchengzi, Wulong, and Maoling) (Fig. 1b). The gold deposits occur within auriferous quartz veins hosted by Mesozoic granites (e.g., Wulong), and within altered Paleoproterozoic metamorphic rocks (e.g., Baiyun, Xiaotongjiapuzi, Maoling, and Sidaogou) (Fig. 1b). The Baiyun gold deposit is located within the northern Qingchengzi orefield.

The Qingchengzi Pb–Zn–Au–Ag polymetallic orefield is located in the north of the Liaodong gold province (Fig. 1b). Reserves in the orefield are estimated be ~ 1.5 Mt of Pb and Zn, 2000 t of silver, and 100 t of gold (Yu et al. 2009). The orefield contains 5 gold deposits, 1 silver deposit, and 15 Pb–Zn deposits. The major gold occurrences include the Baiyun, Xiaotongjiapuzi, and Linjiasandaogou deposits (Fig. 2). The detailed geology characteristics have been described by Yu et al. (2009) and Duan et al. (2014, 2017).

Geology of the Baiyun deposit

The strata in the Baiyun gold deposit are composed of the Paleoproterozoic Dashiqiao and Gaixian formations (Fig. 3). The Dashiqiao Formation comprises amphibolite, marble, and tremolite schist, whereas the Gaixian Formation comprises marble, granulite, and schist. Quartz porphyry, diorite porphyry, and lamprophyre dikes intrude the Paleoproterozoic metamorphic units (Fig. 3). The quartz porphyry dikes typically occur along E–W-trending faults and are generally confined to the hanging wall of the orebodies (Figs. S1a, b). The quartz porphyry contains 10 vol% subhedral to euhedral quartz phenocrysts (0.1–1.0 mm) in a fine-grained groundmass (0.02–0.04 mm) of quartz and plagioclase. Adjacent to ore veins, quartz porphyry is pyritized and sericitized (Figs. S1c, d). Unaltered microdiorite dikes striking NW–SE and E–W cross-cut orebodies within the Baiyun deposit (Figs. S1e, f). These dikes post-date mineralization and comprise plagioclase, quartz, amphibole, and biotite.

The Baiyun deposit contains gold reserves of > 20 t, and more than 20 orebodies have been identified, with gold grades ranging from 1.20 to 42.0 g/t (mean = 5.86 g/t). The orebodies occur primarily within altered sillimanite–biotite schist and granulite of the Gaixian Formation. Most orebodies dip south at 30° to 40°. Two styles of gold mineralization are observed in the Baiyun deposit. The dominant type is altered rock ore

Fig. 1 Regional geology of the study area. **a** Map of the China Craton and distribution of major gold deposits in several gold districts (after Zhu et al. 2015). **b** Geological map of Liaodong region showing the location of major deposits

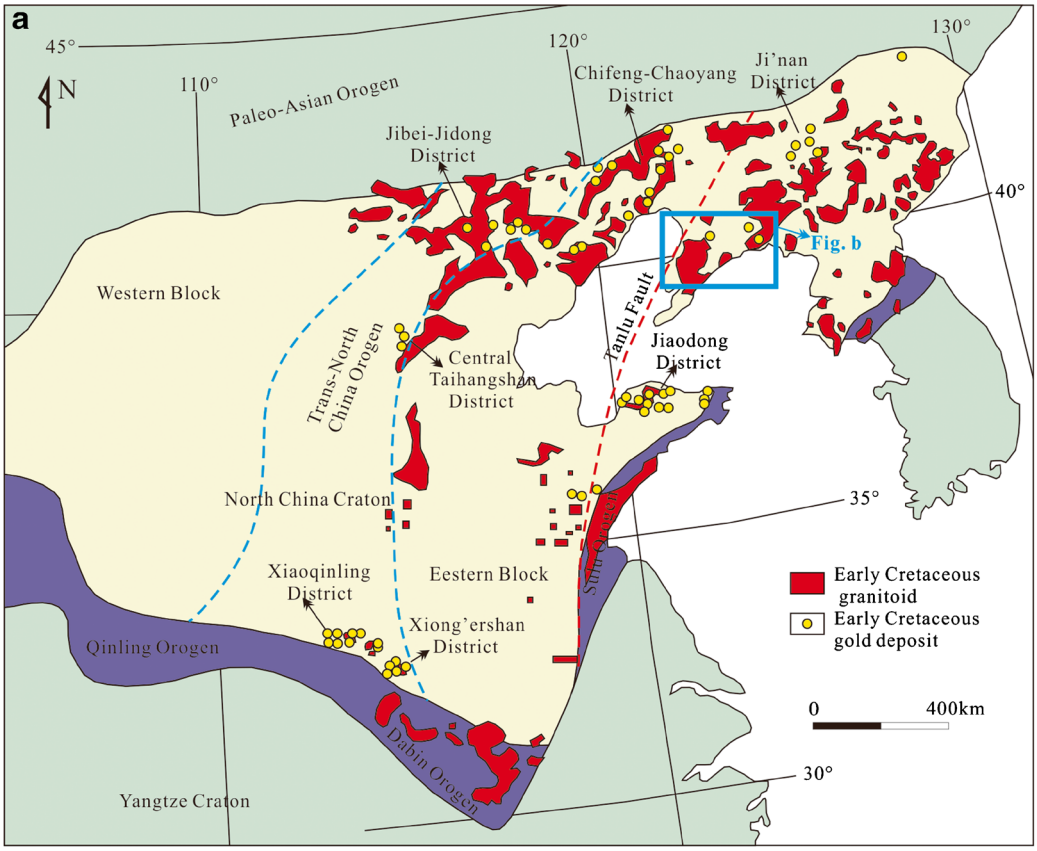
a
45°
110°
120°
130°
40°
35°
30°
N
Paleo-Asian Orogen
Chifeng-Chaoyang District
Ji'nan District
Jibei-Jidong District
Fig. b
Western Block
Tanlu Fault
Trans-North China Orogen
Central Taihangshan District
Jiaodong District
North China Craton
Sulu Orogen
Xiaoqinling District
Eestern Block
Xiong'ershan District
Qinling Orogen
Dabie Orogen
Yangtze Craton
Early Cretaceous granitoid
Early Cretaceous gold deposit
0 400km

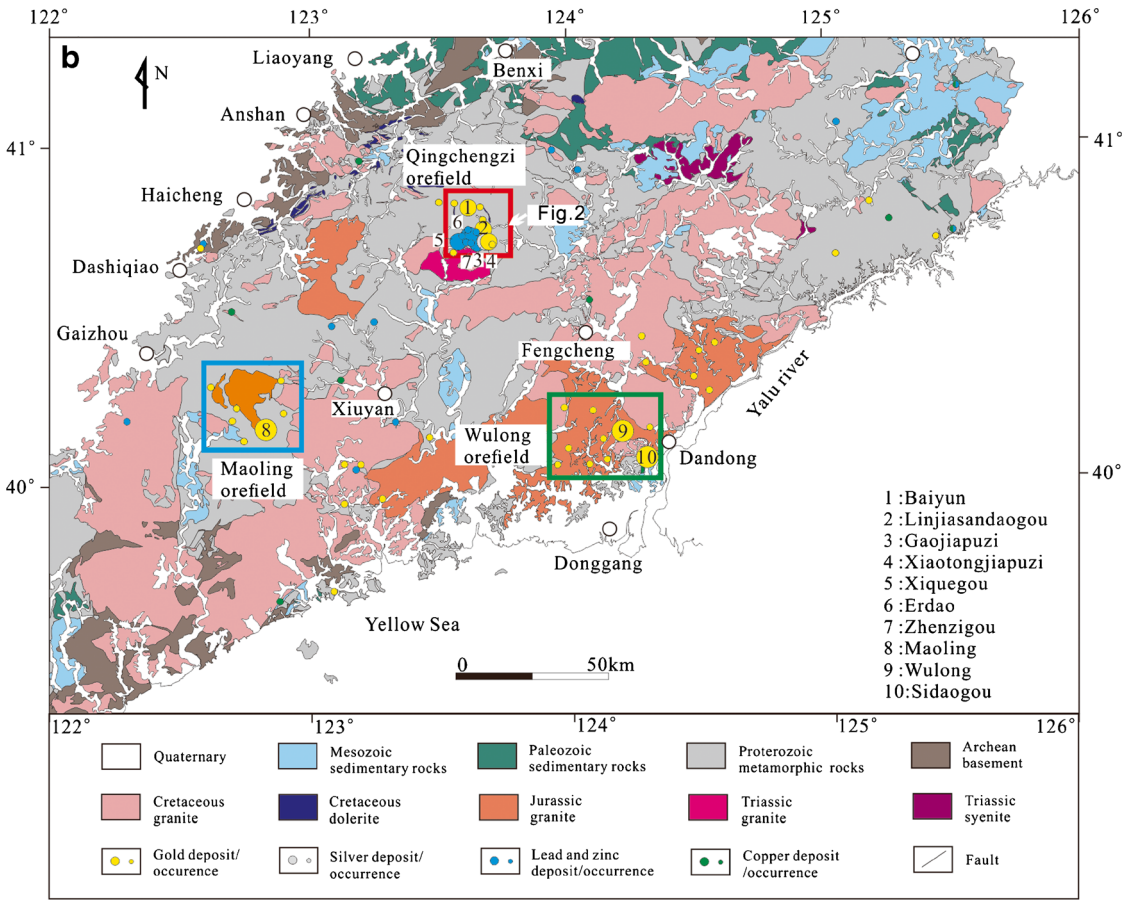
b
122°
123°
124°
125°
126°
41°
40°
N
Liaoyang
Benxi
Anshan
Qingchengzi orefield
Haicheng
Fig.2
Dashiqiao
Gaizhou
Fengcheng
Yalu river
Xiuyan
Wulong orefield
Maoling orefield
Dandong
Donggang
Yellow Sea
0 50km
1 :Baiyun
2 :Linjiasandaogou
3 :Gaojiapuzi
4 :Xiaotongjiapuzi
5 :Xiquegou
6 :Erdao
7 :Zhenzigou
8 :Maoling
9 :Wulong
10:Sidaogou
Quaternary
Mesozoic sedimentary rocks
Paleozoic sedimentary rocks
Proterozoic metamorphic rocks
Archean basement
Cretaceous granite
Cretaceous dolerite
Jurassic granite
Triassic granite
Triassic syenite
Gold deposit/ occurence
Silver deposit/ occurrence
Lead and zinc deposit/occurrence
Copper deposit /occurrence
Fault

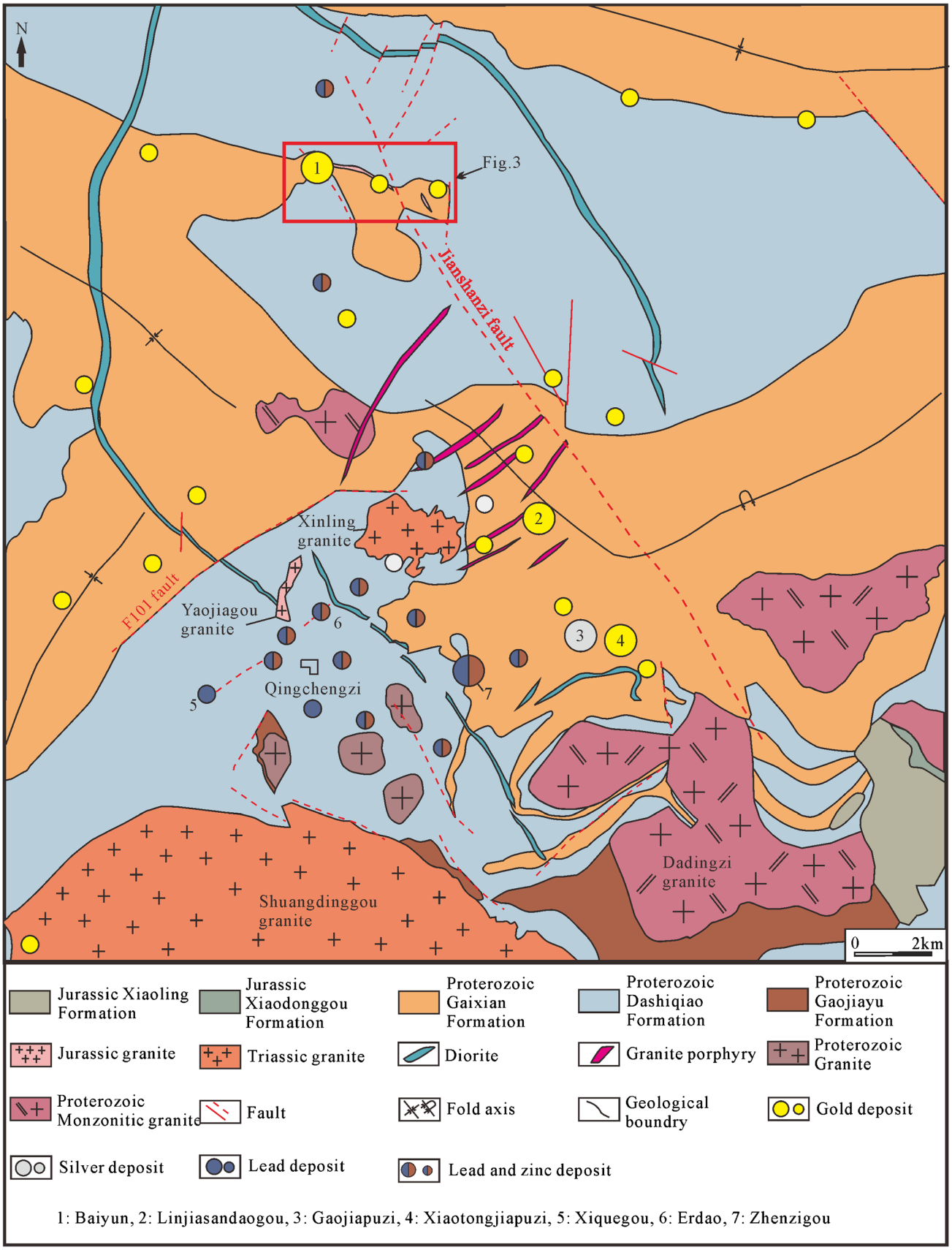

Fig. 2 Geological map of Qingchengzi district showing the location of major deposits (the square shows the location of Baiyun deposit)

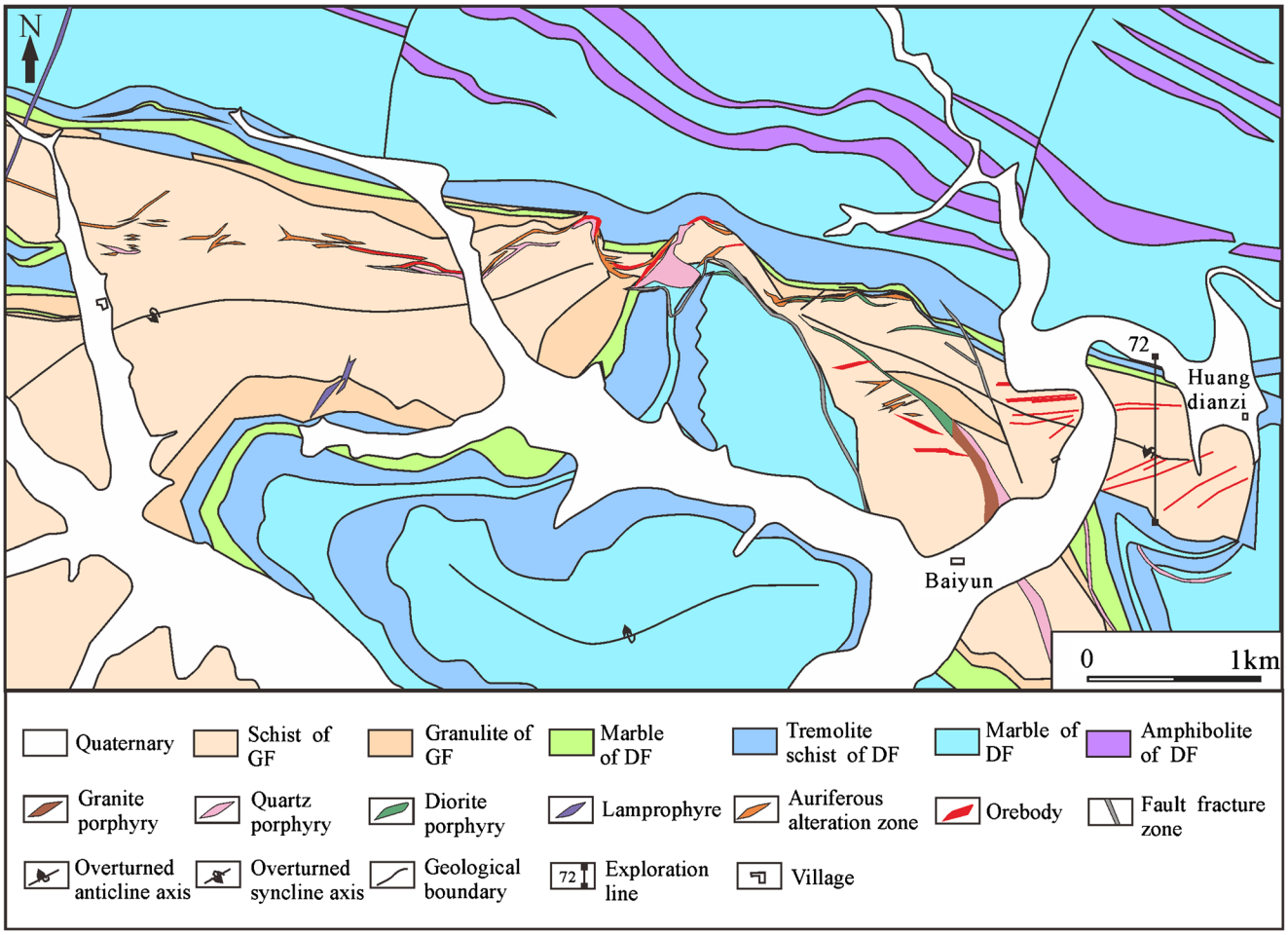

Fig. 3 Geological map of Baiyun gold deposit (after Liaoning Zhaojin Baiyun gold Mining Corporation). GF, Gaixian Formation; DF, Dashiqiao Formation

(e.g., the No. 1, 2, and 11-4 veins) (Fig. 4a, b). These orebodies typically occur as veins (without quartz veins) and are spatially associated with faults that dip 30°–40° toward south. The minor mineralization occurs in auriferous quartz veins (e.g., the No. 60-2 vein) (Fig. 4c), and these veins show different types of quartz (Fig. 4d). Auriferous quartz veins are mainly controlled by faults dipping 30°–40° toward southeast. Characteristics of the major orebodies are listed in Table 1.

Alteration mineralogy

Host rocks associated with gold mineralization were extensively altered by fluids, resulting in vein formation and gold precipitation. In schists far from the ore veins, relict primary metamorphic minerals are preserved (Fig. S2). Adjacent to ore veins, schists are pervasively sericitized (Ser1) (Figs. S2b–d), and alteration produced quartz (during silicification related to vein-stage Qz1) (Figs. S2a–c), muscovite (Ms1) (Fig. S2d), and chlorite (Chl1) (Fig. S2e). Evidence for minor carbonation is also observed (Figs. S2a, f). The altered schists contain 2–5 vol% pyrite and trace amounts of chalcopyrite, mainly as blebs within pyrite grains. Pyrite grains are typically disseminated, or locally form polycrystalline masses or bands.

Mineral paragenesis and mineralization stages

In the Baiyun gold deposit, the dominant hydrothermal minerals are quartz, sericite, and pyrite, with lesser amounts of calcite, barite, chalcopyrite, gold, and hessite (Figs. 4 and 5). Gold is present as electrum and is concentrated within quartz veins and altered rocks. Fine-grained electrum (5–70 μm) has an Au/Ag ratio from 67:33 to 75:25 (at.%). Three mineralization stages have been identified in the Baiyun deposit, based on crosscutting relationships, and mineralogical and textural characteristics (Fig. 6): pyrite–quartz (stage 1), pyrite–quartz–chalcopyrite (stage 2), and quartz–carbonate (stage 3).

Stage 1 mineralization is characterized by quartz–pyrite veins comprising coarse-grained quartz (Qz1) (94%) and pyrite (Py1) (6%). The thickness of these veins range from 0.2 to 2.0 m. Coarse (1–3 cm) crystals of quartz are milky. Pyrite 1 (Py1) is (0.2–5.0 cm), subhedral to euhedral, commonly fractured, and is typically disseminated within the vein (Fig. 4d).

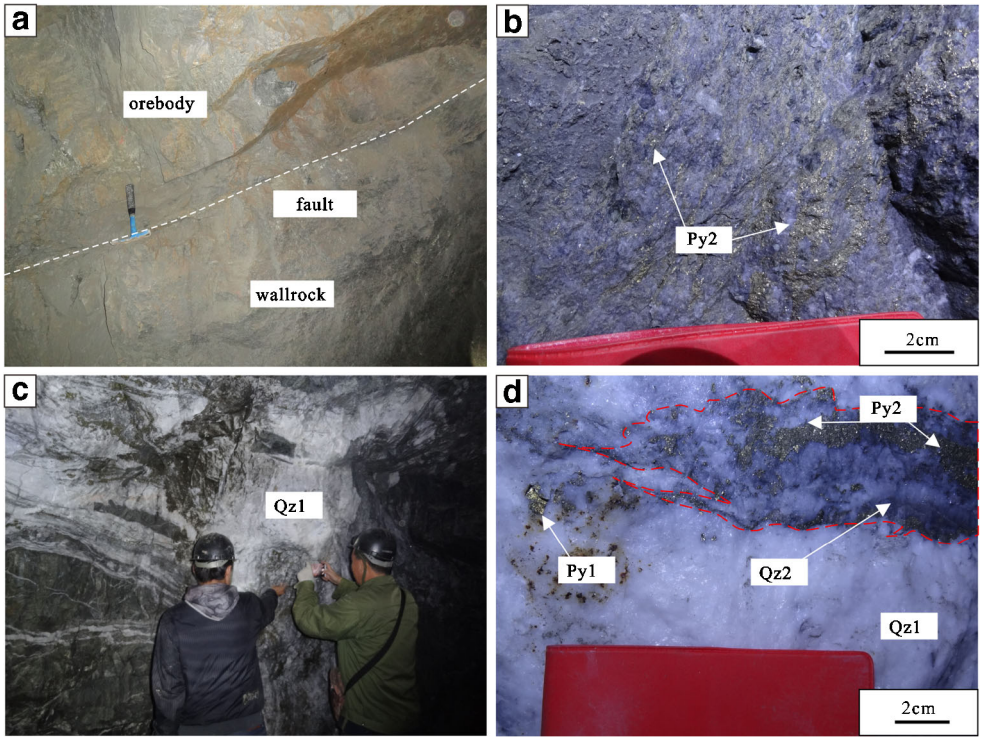

Fig. 4 Field view photographs showing crosscutting relationships of the geologic bodies from the Baiyun deposit. **a** Underground photograph of the Baiyun deposit 11-4 vein on level 280 m. **b** Underground photograph of the Baiyun deposit 11-4 vein on level 280 m displaying alteration-type orebodies. **c** Underground photograph of the Baiyun deposit 60-2 vein on level 100 m displaying extensional veins. **d** Stage 2 quartz (Qz2)-pyrite (Py2) veins crosscutting the primary quartz (Qz1)-pyrite (Py1) vein. Qz, quartz; Py, pyrite

Some of electrum post-date Py1 as it is dominantly observed as veinlets along fractures in Py1 (Fig. 5c–e) and along Py1 boundaries (Fig. 5b). These gold-bearing veins cut altered schists along brittle fractures.

Stage 2 mineralization is characterized by quartz–pyrite–chalcopyrite veinlets and stockworks within stage 1 ore minerals, and consists of fine-grained quartz (Qz2), fine-grained pyrite (Py2), and chalcopyrite. The thickness of these veins ranges from 0.2 to 8.0 cm. Finer gray quartz grains (< 0.2 mm; Qz2) are observed within veins that crosscut Qz1 veins (Fig. 4d). Finer-grained pyrite (< 1 mm; Py2) occurs coexisting with Qz2 veins that crosscut Qz1 veins (Fig. 4d). Py2 is intergrown with Qz2, which may together represent a second hydrothermal event. Electrum occurs as inclusions in Py2 or is intergrown with Qz2 (Fig. 5f, d). In alteration-related ore bodies, hessite (Ag_2Te) is present as inclusions within Py2 (Fig. 5g, h).

Stage 3 mineralization is characterized by quartz–carbonate veinlets that cut veins and alteration zone related to stages 1 and 2. Barite can also be observed in these veinlets. Gold is not associated with this stage of mineralization.

Samples and analytical methods

Microthermometry and Raman spectroscopy

We analyzed 67 samples of mineralized schist and quartz veins from the Baiyun deposit, which were prepared as polished thin sections, as well as 54 fluid inclusion plates. Fluid inclusion microthermometry was conducted using a Linkam THMSG 600 heating–freezing stage (− 198 to 600 °C) and a Leitz microscope at Fluid Inclusion Laboratories, China University of

Table 1 Features of the major orebodies from the Baiyun deposit

Orebody	Type	Tendency (°)	Dip angle (°)	Highest grade (g/t)	Lowest grade (g/t)	Average grade (g/t)	Minimum thickness (m)	Maximum thickness (m)	Length (m)
No. 1	Altered rock	180–190	30–40	8.2	1.0	6.7	1.0	3.5	1300
No. 11-4		180–190	30–40	4.8	1.3	2.3	1.0	28.2	500
No. 60-1		190–200	30–45	4.2	1.0	1.8	1.2	7.4	400
No. 60-2	Auriferous quartz veins	140–150	20–30	40.0	1.1	3.5	1.5	10.9	200

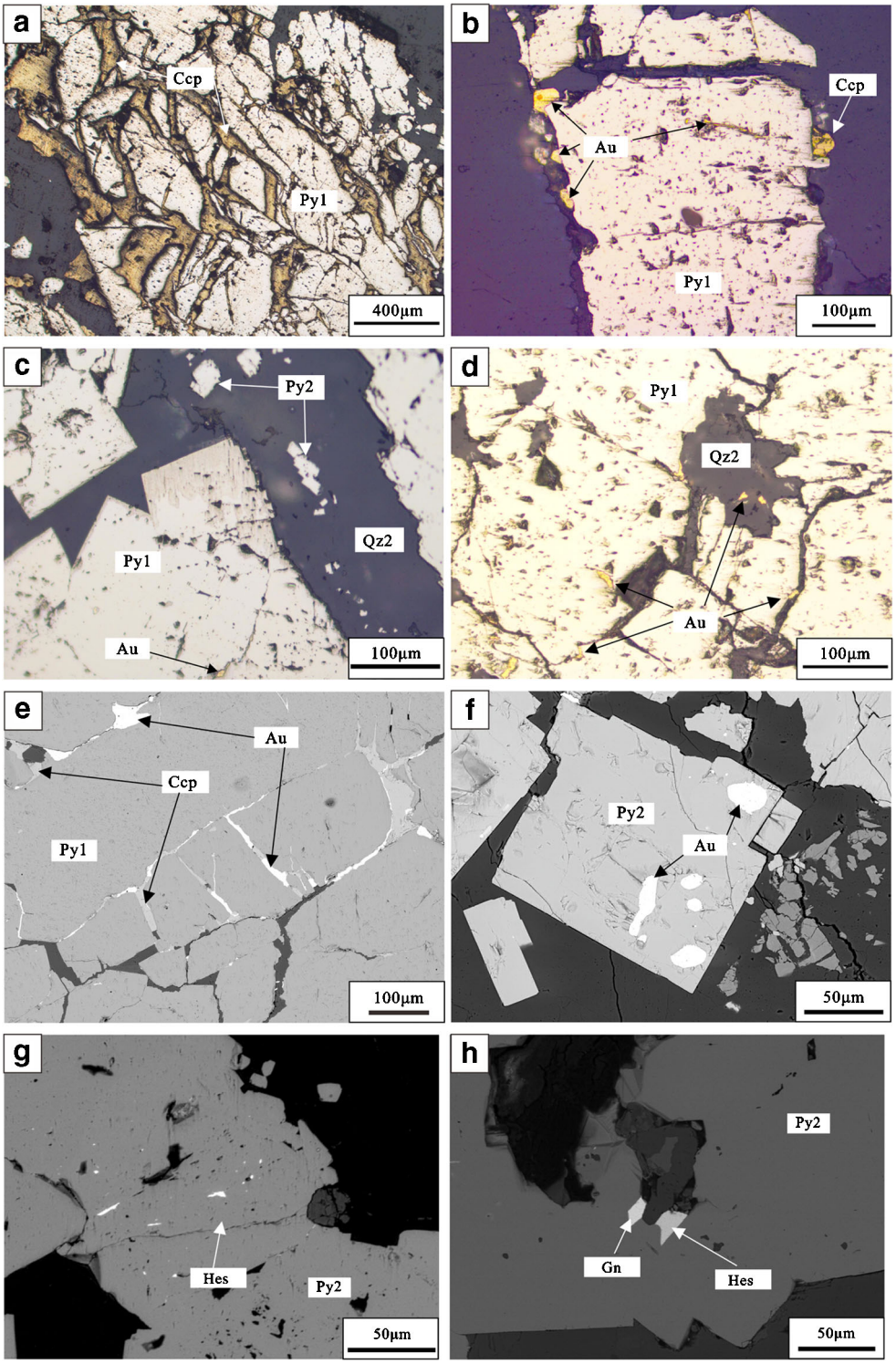

Fig. 5 Photomicrographs and BSE images showing textural relationships between electrum and other vein minerals from the Baiyun deposit. **a** Chalcopyrite occurring along primary pyrite (Py1) fractures. **b** Chalcopyrite and electrum occurring along primary pyrite (Py1) boundaries. **c** Electrum occurring along fractures of Py1, Qz2-Py2 vein crosscutting Py1. **d** Electrum occurring along Py1 boundaries and fractures or hosted by secondary quartz (Qz2). **e** Chalcopyrite-electrum veins crosscutting Py1 (BSE image). **f** Electrum occurring as inclusions within Py2 (BSE image). **g** Py2 containing inclusions of hessite (BSE image). **h** Hessite and galena occurring as wedge shaped in Py1 (BSE image). Ccp, chalcopyrite; Py, pyrite; Au, electrum; Qz, quartz; Hes, hessite; Gn, galena

Geosciences, Beijing, China. Synthetic fluid inclusions were used to calibrate the stage to ensure the measurement accuracy. Most measurements were made using a heating rate of 0.2–0.5 °C/min. The temperatures of solid CO_2 phase melting (T_{mCO2}) and CO_2 clathrate melting (T_{mclath}) were determined by temperature cycling (Roedder 1984; Diamond 2001); the heating rate at temperatures close to T_{mCO2} and T_{mclath} was set at 0.1–0.2 °C/min. The stage uncertainty is ± 0.1 °C for temperatures below 30 °C and ± 1 °C for homogenization temperatures. The salinity of H_2O–Na_2Cl and H_2O–NaCl–CO_2 fluid inclusions was determined as follows: $W_{NaCl} = 0.00 + 1.78T_{mice} - 0.0442T_{mice}^2 + 0.000557T_{mice}^3$ (Hall et al. 1988) and $W_{NaCl} =$

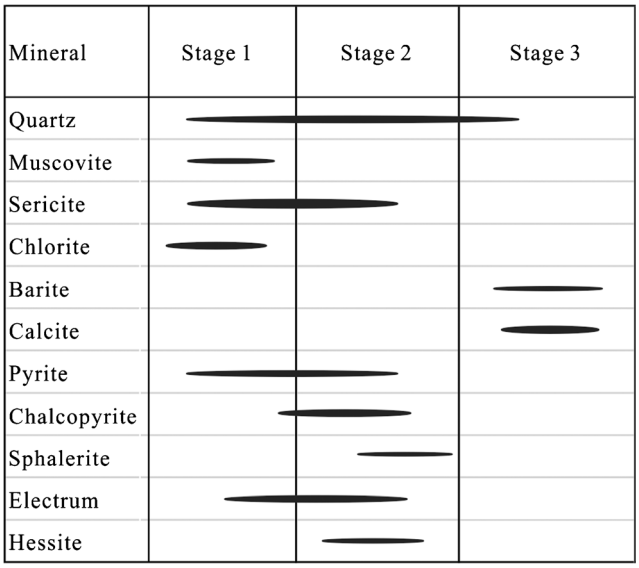

Fig. 6 Paragenesis of gangue and ore minerals at the Baiyun deposit. Line thickness represents relative amount of the minerals

$15.52022–1.02342T_{mclath} - 0.05286T_{mclath}^2$ (Roedder 1984). Fluid inclusions densities were estimated using the equation from Brown and Lamb (1989) by the Flincor software package (Brown 1989). The trapping pressures were estimated using the equation from Bowers and Helgeson (1983) by the Flincor software package.

For Laser Raman spectroscopy, we prepared double-polished thin sections. Analysis was performed at room temperature using a Jobin-Yvon Horiba LabRam HR confocal Raman microscope equipped with an 800-mm spectrograph at the Institute of Geology and Geophysics, Chinese Academy of Science (IGGCAS), Beijing, China.

Oxygen and hydrogen isotope analyses

Oxygen and hydrogen isotope analyses of quartz were performed at the Laboratory for Stable Isotope Geochemistry, IGGCAS. Samples were carefully handpicked under a binocular microscope after the samples had been crushed, cleaned, and sieved to 40 to 60 mesh, resulting in a separate of 99% pure quartz. Oxygen was liberated from quartz by reaction with BrF_5 and converted to CO_2 on a platinum-coated carbon rod. The $\delta^{18}O$ determinations were made using a MAT-252 mass spectrometer. The $\delta^{18}O_{quartz}$ values were corrected using in-house quartz standard GBW04409, with a value of + 11.11 ± 0.06‰ (Cao et al. 2014). Reproducibility for isotopically homogeneous pure quartz is about ± 0.2‰ (1σ). $\delta^{18}O_{water}$ values of ore fluids were calculated using the equation for equilibrium isotope fractionation of oxygen between quartz and water (Clayton et al. 1972).

Analyses of hydrogen isotopic compositions of the fluid inclusions in quartz were carried out on the splits of the samples for oxygen isotope analyses. Weighted amounts of quartz were loaded into a quartz tubes which have been roasted at 800 °C and stored at 110 °C prior to use. Water was released by heating the samples to approximately 500 °C in an induction furnace. Samples were first degassed by heating under vacuum to 120 °C for 3 h. Water obtained by degassing at 500 °C was converted to hydrogen by reaction with heated zinc powder at 410 °C and the hydrogen was analyzed with a MAT-252 mass spectrometer. The δD_{water} values were corrected using water standard GBW04402, with a value of − 64.8 ± 0.11‰ (Cao et al. 2014). The results are reported relative to V-SMOW with analytical uncertainties ± 2‰.

Zircon U–Pb analysis

Two samples were selected for zircon U-Pb analysis in the Baiyun gold deposit. Sample BY-52 is from a pre-ore quartz porphyry, located at the hanging wall of orebodies. Sample BY17-53 is from a post-ore microdiorite that intruded the orebodies. Zircon crystals were obtained using a combination of heavy liquid and magnetic separation techniques. Individual crystals were handpicked and embedded in epoxy resin, and then polished to expose the grain centers. Cathodoluminescence (CL) images were obtained using a JEOL 6510 electron microprobe at Beijing GeoAnalysis, Beijing, China. LA–ICP–MS zircon analyses were conducted at Sample Solution Analytical Technology Corporation, Wuhan, China, using an Agilent 7700 ICP–MS equipped with a GeolasPro 193-nm laser ablation system. A 24–32-μm spot size was used. Background signals were measured with the laser off for 20 s, followed by a data collection period with the laser firing for 50 s. Time-integrated signals, time-drift correction, and quantitative calibration were made using the ICPMSDataCal software package (Liu et al. 2010). Zircon 91500 and GJ-1 were used as standards and the standard silicate glass NIST 610 was used to optimize the instrument. The detailed analytical method has been described by Liu et al. (2010). U, Th, and Pb concentrations were calibrated using ^{29}Si as an internal calibrant and NIST 610 as a reference material. Final interpretation of the analytical results was performed using ISOPLOT software (Ludwig 2003).

Results

Fluid inclusion petrography

Three types of fluid inclusion were observed in quartz and calcite at room temperature. Figure 7 shows the various fluid inclusion types developed in vein stages 1 through 3.

W-type (aqueous type) inclusions are two-phase ($L_{aq} + V_{aq}$) H_2O–NaCl ± CO_2 inclusions hosted in Qz1, Qz2, and calcite (Fig. 7a–d). W-type inclusions hosted in quartz have variable morphologies, are 5–16 μm in size, and have V/L (volume/

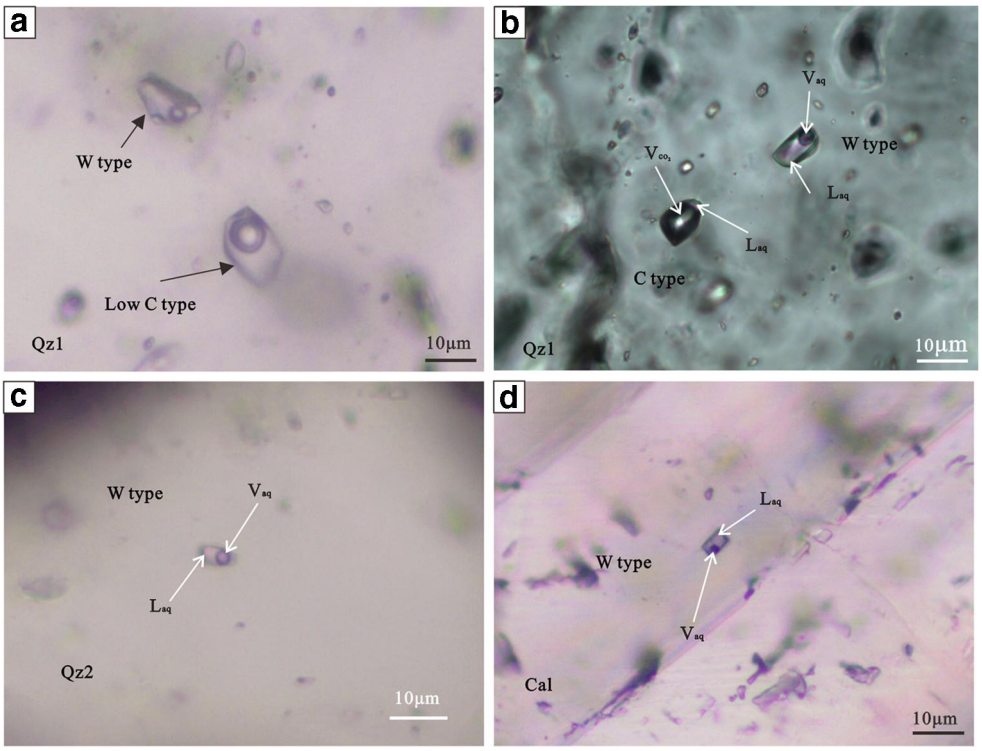

Fig. 7 Photomicrographs showing petrographic characteristics of fluid inclusions. **a** Low C-type and W-type inclusions in Qz1. **b** W-type (L_{aq} + V_{aq}) and C type (L_{aq} + V_{co2}) inclusions in Qz1. **c** W-type inclusion in Qz2. **d** W-type inclusions in calcite. L_{aq}, liquid aqueous phase; L_{co2}, liquid carbonic phase; V_{co2}, vapor carbonic phase; V_{aq}, vapor aqueous phase

liquid) ratios of 0.1–0.4. W-type inclusions in calcite have oval or rectangular shapes, range in size from 4 to 8 μm, and have V/L ratios of 0.1–0.3.

Low C-type (low carbonic type) inclusions are three-phase (L_{aq} + L_{CO_2} + V_{CO_2}) H_2O–NaCl–CO_2 inclusions hosted in Qz1 and Qz2 (Fig. 7a). The inclusions have rectangular, oval, or circular shapes; show no evidence of decrepitation or necking down; and range in size from 5 to 20 μm. Low C-type inclusions typically occur in clusters, but are also observed along linear features interpreted as healed fractures. The volume of the carbonic phase, 25–50 vol%, is relatively consistent in each assemblage. The proportion of L_{CO_2} to V_{CO_2} (and the corresponding CO_2 homogenization temperature) is similar for all assemblages.

C-type (carbonic type) inclusions are two-phase (L_{aq} + V_{CO_2}) CO_2 ± CH_4 ± N_2 ± H_2O inclusions hosted in Qz1 within stage 1 veins (Fig. 7b). These inclusions generally have oval or rectangular shapes and are 8–12 μm in size. The vapor phase typically occupies ~ 90 vol% and the L_{aq} phase coats the inclusion walls (Fig. 7b).

Fluid inclusion study

Microthermometry results are listed in Table 2. Microthermometric data were obtained from low C-type and W-type inclusions. The C-type inclusions are not common. Microthermometric data were not collected as inclusions commonly decrepitated.

Stage 1

Most inclusions hosted in Qz1 are W-type liquid-rich, two-phase, aqueous inclusions. Inclusions homogenized to liquid between 230 and 289 °C (Fig. 8). Salinities range from 3.4 to 16.5 wt%

Table 2 Microthermometric data for fluid inclusions of the Baiyun deposit

Stage	Type	Origin	Number	T_{mclath} (°C)	T_{mice} (°C)	T_{hCO2} (°C) (V to L)	T_{hTOT} (°C) (V to L)	Salinity (wt% NaCl equiv.)	CO_2 density (g/cm^3)	Bulk density (g/cm^3)
1	1	P or Ps	30	6.1–8.3		28.8–30.3	261–285	3.4–7.5	0.58–0.64	0.83–0.93
	2	P or Ps	27		−12.0–-2.1		230–289	3.4–16.5		0.82–0.94
2	1	P	3	5.5–6.0		26.0–30.2	241–253	7.5–8.3	0.58–0.70	0.82–0.89
	2	P	50		−12.9–-5.7		203–259	5.7–16.8		0.84–0.97
3	2	P	27		−10.5–-0.1		138–208	0.2–14.5		0.90–1.00

V to L means that inclusions homogenized to liquid. *P*, primary; *Ps*, pseudosecondary

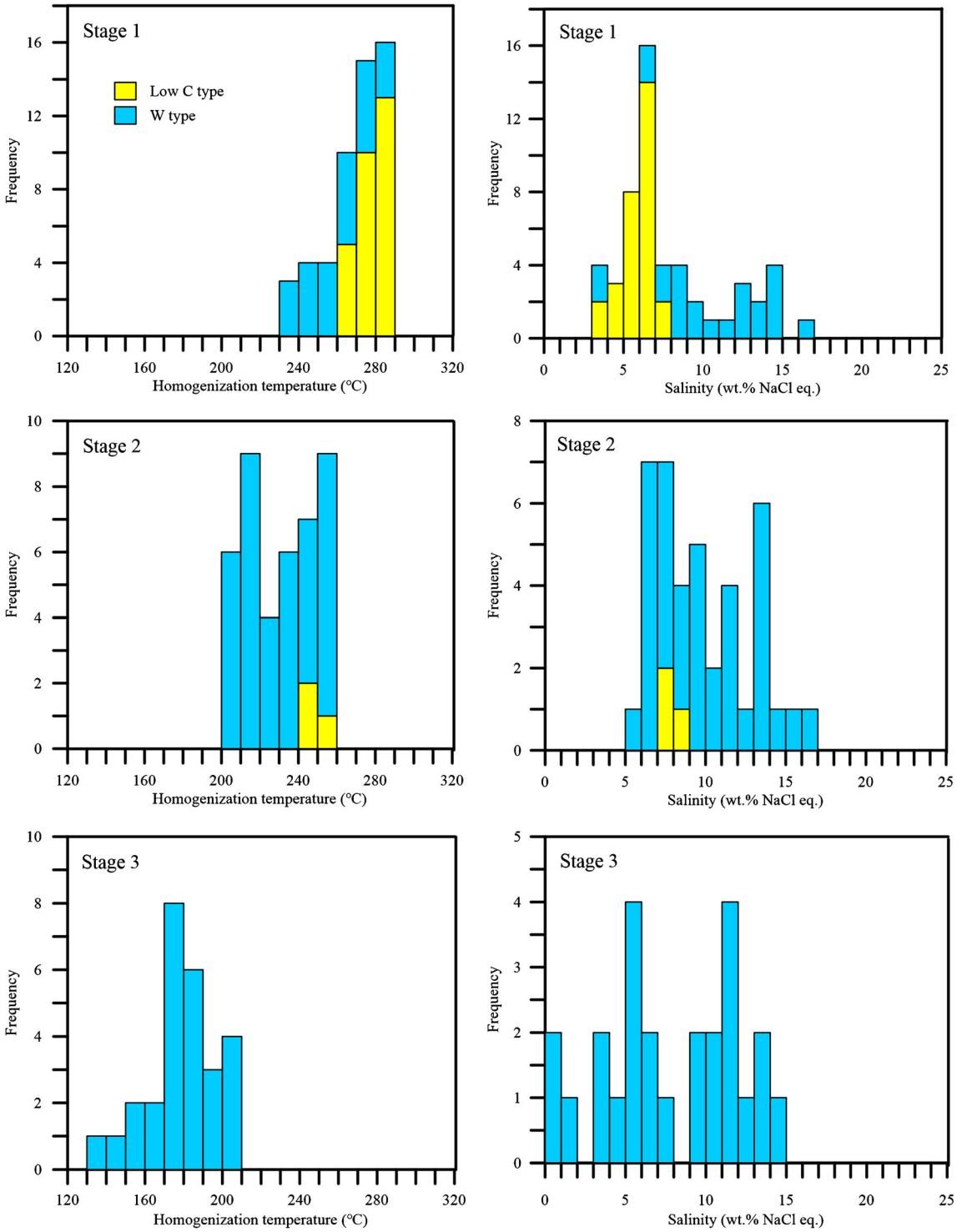

Fig. 8 Histograms of total homogenization temperature (T_h) and salinities of fluid inclusions in different stages

NaCl eq.; a strong mode occurs between 7 and 15 wt% NaCl eq. (Fig. 8). Neither clathrate formation nor CO_2 ice melting were observed, indicating that CO_2 constitutes less than 4 mol% of the fluid (Hedenquist and Henley 1985). Low C-type three-phase, H_2O–CO_2 inclusions yielded T_{mCO2} from − 57.2 to − 56.6 °C, indicating the lack of other gases. T_{mclath} of 6.1–8.3 °C indicate low fluid salinities ranging from 3.4 to 7.5 wt% NaCl eq. CO_2 phases homogenized to liquid at 28.8–30.3 °C, indicating a range of CO_2 densities from 0.58 to 0.64 g/cm^3. Total homogenization (T_{hTOT}) to liquid occurred at 261–285 °C (Fig. 8).

Stage 2

Qz2 contains dominantly W-type and rare low C-type fluid inclusions. W-type inclusions yielded T_{hTOT} of 203°–259 °C (Fig. 8). Inclusions have salinities from 5.7 to 16.8 wt% NaCl eq. Low C-type inclusions yield T_{mCO2} between − 57.4 and − 56.8 °C, indicating CO_2 was the only gas. Clathrate melting varied from 5.5 to 6.0 °C, indicating fluid salinities between 7.5 and 8.3 wt% NaCl eq. T_{hCO2} was between 26 and 30.2 °C, indicating that CO_2 densities range from 0.82 to 0.89 g/cm^3. Inclusions homogenized to liquid from 241 to 253 °C (Fig. 8).

Stage 3

W-type inclusions in calcite have salinities range from 0.2 to 14.5 wt% NaCl eq and exhibit two modes at 3.0–8.0 wt% NaCl eq and 9.0 to 15.0 wt% NaCl eq. W-type inclusions homogenized by vapor bubble disappearance at temperatures between 138 and 208 °C (Fig. 8).

Laser Raman spectroscopy of inclusion gases

Low C-type inclusions from stages 1 contain a CO_2 vapor phase, without CH_4 (Fig. 9a). C-type inclusions from stage 1 show well-defined CO_2, CH_4, and N_2 peaks (Fig. 9c). W-type inclusions from stages 1 and 2 contain traces of CO_2 and CH_4 vapor phases (Fig. 9b–f).

Oxygen and hydrogen isotopes

Table 3 lists oxygen and hydrogen isotope ratios obtained from Qz1, and calculated $\delta^{18}O_{water}$ values of ore fluids. The $\delta^{18}O_{water}$ from stage 1 are close to the primary magmatic water (5.5 ‰ to 10 ‰; Taylor 1974). The δD from stage 1 also approach to that of the primary magmatic water (− 80 to − 40‰; Taylor 1974) and deviate from the range of the metamorphic water (− 65 to − 20‰; Taylor 1974).

Zircon U–Pb geochronology

CL images of zircons are shown in Fig. 10. Results of U–Pb zircon analyses are shown in Fig. 10 and listed in Table 4. Zircons selected from sample BY-52 range in size from 50 to 130 μm and are pale brown in color. Most grains are euhedral, and their aspect ratios vary from 2:1 to 3:1 (Fig. 10a). Nine euhedral zircon grains yield ages from 129 to 127 Ma (Table 4). These analyses form a coherent group and yield a weighted mean $^{206}Pb/^{238}U$ age of 127.8 ± 0.8 Ma (MSWD = 0.17; Fig. 10c).

Zircon grains selected from Sample BY17-53 range in size from 70 to 130 μm. Most grains are subhedral, and their aspect ratios vary from 2:1 to 4:1 (Fig. 10b). Twenty-three subhedral zircon grains yield ages ranging from 2454 to 123 Ma (Table 4). The inherited zircons show ages between 2454 and 202 Ma. These ages are consistent with the Liaohe Group and Triassic intrusions in this region (Lu et al. 2006). The remaining 12 analyses form a coherent group and yield a weighted mean $^{206}Pb/^{238}U$ age of 125.6 ± 1.3 Ma (MSWD = 0.5; Fig. 10d).

Discussion

Ore formation and gold deposition inferred from fluid inclusions

Fluid inclusion data can be used to constrain the pressure–temperature evolution of ore fluids during gold mineralization in lode-gold deposits (Wilde et al. 2001; Wang et al. 2015c; Chai et al. 2016; Neyedley et al. 2017). In the Baiyun deposit, three stages of hydrothermal minerals are identified, and they contain distinct fluid inclusion assemblages that can be used to trace the evolution of the ore fluid.

Stage 1 quartz veins contain W-type, low C-type, and minor C-type inclusions. The variable CO_2:H_2O ratios in coexisting inclusions (Fig. 7a, b) could have induced by mixing or un-mixing of two immiscible fluids (Anderson, et al. 1992) or through post-entrapment modifications. The lack of a continuum in degree of filling of the mixed CO_2–H_2O inclusions and absence of homogenization into vapor may rule out the immiscibility as a potential mechanism in the Baiyun deposit (Wang et al. 2015c; Chai et al. 2016; Neyedley et al. 2017). Absence of a vertical trend in T_{Htot} versus salinity correlation, which is typical for necking down and leakage during heating, discards the selective water loss via diffusion in measured inclusions. Mixing of fluids is suggested by a salinity change of aqueous fluid inclusions at a near-constant temperature (Lécuyer et al. 1999). Evidence of mixing is also stipulated by the occurrence of discrete clusters of relatively low-salinity low C-type inclusions close to moderate salinity aqueous inclusions. Two distinct fluids can be distinguished based on the fluid inclusion studies. The inferred ore fluid was a moderate salinity fluid that had a temperature of 230–290 °C and contained little CO_2 and CH_4. The other fluid was carbonic aqueous, moderate temperature, low salinity, and without CH_4. We therefore infer that the formation of stage 1 quartz veins was due to fluid mixing of a moderate salinity, reduced ore fluid with a carbonic aqueous, and oxidized fluid.

Fluid mixing has been invoked to explain the deposition of gold in several gold deposits (Hofstra et al. 1991; Cline and Hofstra 2000). The presence of strong silicification and sericitization indicates that the hydrothermal fluids were slightly acidic (Mikucki 1998). In such fluids, gold is transported as gold bisulfide complexes [Au(HS)–2, $Au(HS)^0$] (Seward 1973; Hayashi and Ohmoto 1991;

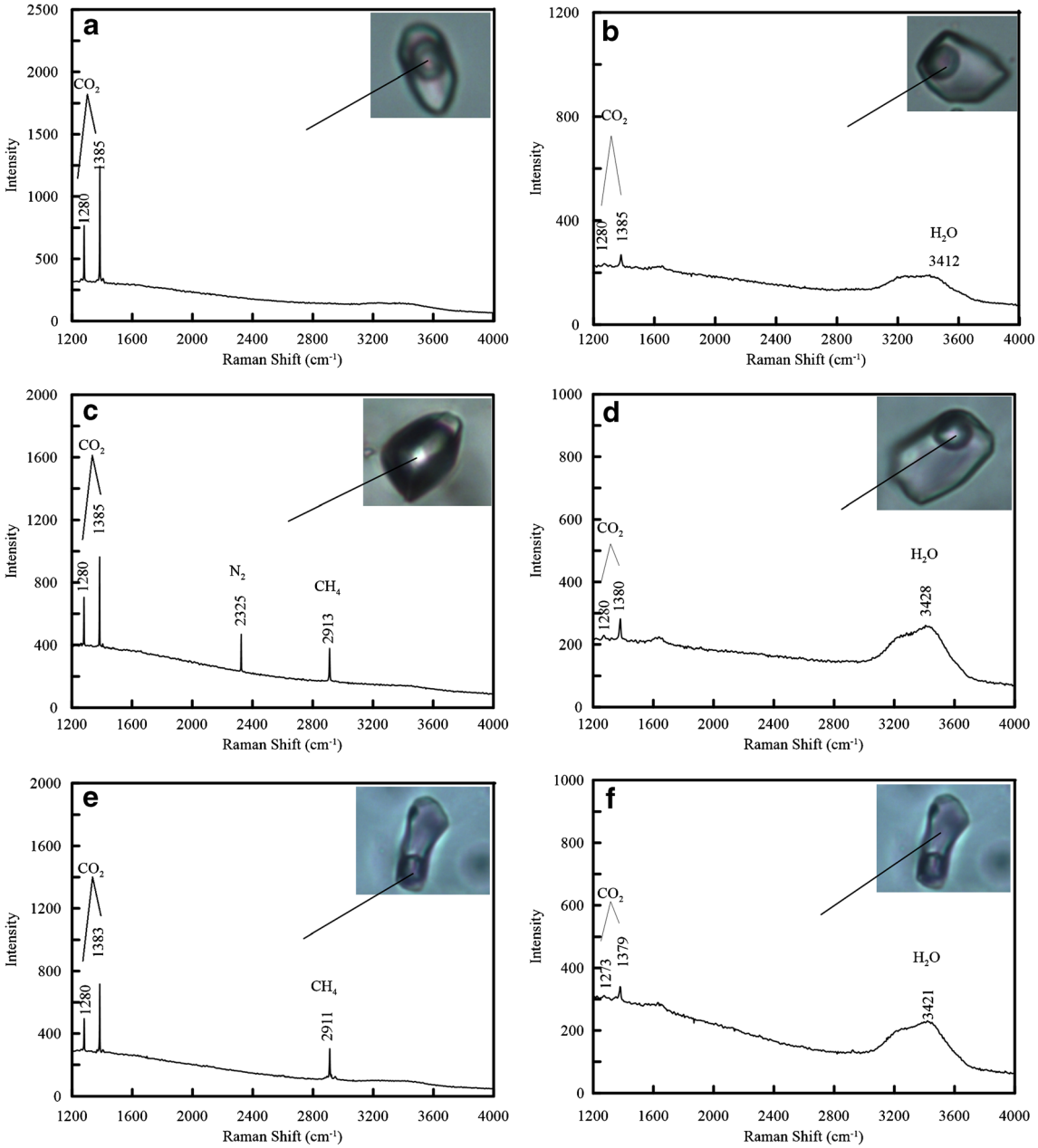

Fig. 9 Representative laser Raman spectra of fluid inclusions. **a** Carbonic phase in low C-type inclusions hosted in Qz1. **b** The H_2O vapor phase in W-type inclusions hosted in Qz1. **c** Carbonic phase in C-type inclusions hosted in Qz1. **d** The H_2O liquid phase in W-type inclusions hosted in Qz1. **e** The H_2O vapor phase in W-type inclusions hosted in Qz2. **f** The H_2O liquid phase in W-type inclusions hosted in Qz2

Zezin et al. 2007). Fluid mixing with a second fluid having a relatively lower concentration of H_2S would dilute the ore fluid, decreasing the H_2S concentration (Arehart 1996). A significant decrease of H_2S from ore fluids results in the destabilization of gold bisulfide complexes (Mikucki 1998). Furthermore, mixing with the oxidized fluid can result in a sharp decrease in bisulfide concentrations. The decrease in bisulfide concentrations drove Reactions (1) and (2) (Tombros et al. 2007) to the right side and resulted in the precipitation of hessite and native gold.

$$\mathrm{HTe}\text{–}(aq) + 2\mathrm{Ag(HS)}\text{–}2(aq) = \mathrm{Ag_2Te}_{(s)} + 4\mathrm{HS}\text{–}(aq) + \mathrm{H} + (aq) \quad (1)$$

$$2\mathrm{H_2O}_{(l)} + 4\mathrm{Au(HS)}\text{–}2(aq) = 4\mathrm{Au}_{(s)} + \mathrm{O}_{2(g)} + 4\mathrm{H} + (aq) + 8\mathrm{HS}\text{–}(aq) \quad (2)$$

Fluid inclusions from stage 2 have a wide range of salinities, indicating that fluid mixing is still the main process. The homogenization temperatures of fluid inclusions from stage 2 are lower than those from stage 1, illustrating that fluid

Table 3 Oxygen and hydrogen isotope analyses in the Baiyun deposit

Sample number	Stage	Mineral	δD (‰)$_{SMOW}$	$\delta^{18}O_{quartz}$ (‰)$_{SMOW}$	$\delta^{18}O_{water}$ (‰)$_{SMOW}$	Temperature (°C)	Reference
BY-21	1	Quartz	− 70	12.7	5.0	280	This study
BY-27	1	Quartz	− 70	11.6	3.9	280	This study
BY-31	1	Quartz	− 69	13.2	5.5	280	This study
BY-39	1	Quartz	− 78	13.1	5.4	280	This study
97–73-1	1	Quartz	− 74	13.9	6.2	300	Liu and Ai 1999
97–73	1	Quartz	− 86	15.5	7.8	300	Liu and Ai 1999
97–72	1	Quartz	− 92	13.5	5.8	300	Liu and Ai 1999
BYHO6	3	Quartz	− 101	14.7	3.0	200	Hao et al. 2017
BYHO7	3	Quartz	− 103	14.7	3.0	200	Hao et al. 2017
BYHO8	3	Quartz	− 100	15.8	4.1	200	Hao et al. 2017
BYHO9	3	Quartz	− 104	14.5	2.8	200	Hao et al. 2017
BYHO10	3	Quartz	− 107	15.6	3.9	200	Hao et al. 2017
BYHO11	3	Quartz	− 96	15.9	4.2	200	Hao et al. 2017
BYHO12	3	Quartz	− 105	15.3	3.6	200	Hao et al. 2017

cooling occurred during stage 2. However, the stability for gold bisulfide complexes change very little with temperature over the range 150–300 °C (Seward 1973; Hayashi and Ohmoto 1991). Therefore, we suggest that fluid mixing may be responsible for the deposition of the gold during stage 2.

During stage 3, the ore fluid was dominated by H_2O–NaCl. W-type inclusions that were trapped during stage 3 yield relatively low homogenization temperatures and salinities, with trends toward lower values (Fig. 11). These data are consistent with mixing of the ore fluid with dilute meteoric water, which typically has a low salinity and temperature. In conclusion, fluid mixing might have triggered the formation of quartz–carbonate veins.

Ore-forming temperature and pressure

For the fluid inclusions, the T_{hTOT} serves only as minimum constrains on the entrapment temperature (Diamond 2001). Therefore, the measured T_{hTOT} values yield the minimum

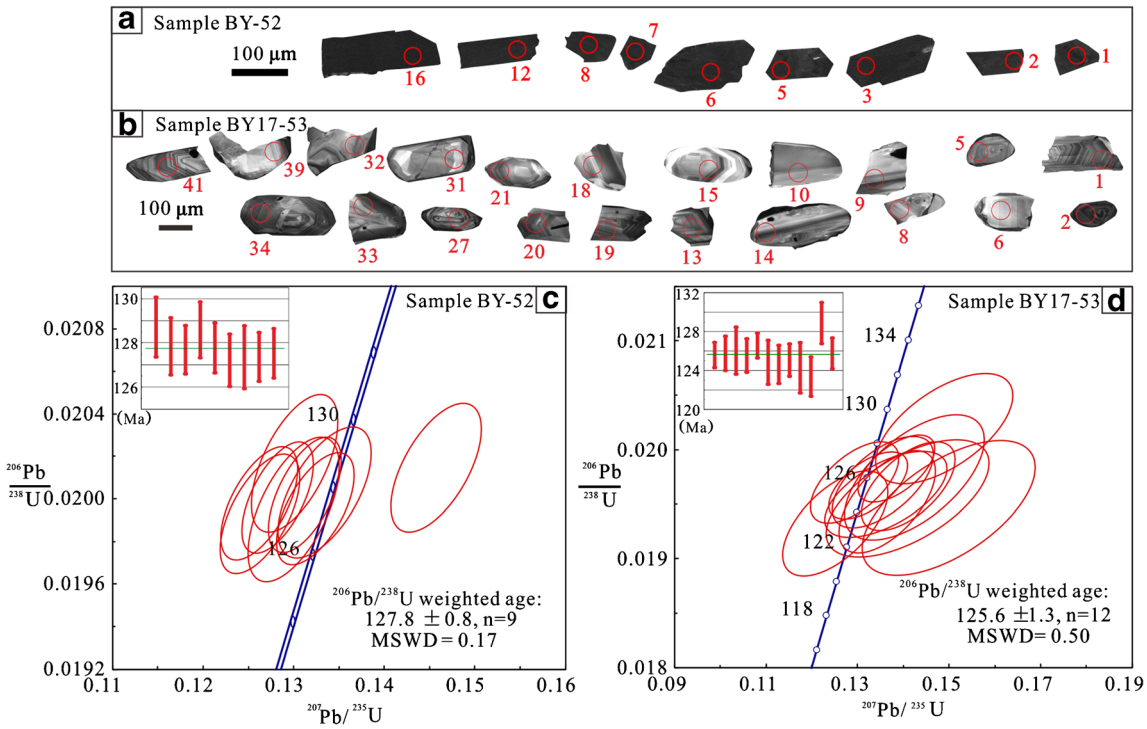

Fig. 10 CL images of zircons and zircon LA-ICP-MS diagrams for the dikes from the Baiyun deposit

Table 4 LA-ICP-MS U-Pb zircon data for dykes from the Baiyun deposit

Spot analysis	Isotopic ratios							Isotopic ages (Ma)	
	$^{207}Pb/^{206}Pb$	1σ	$^{207}Pb/^{235}U$	1σ	$^{206}Pb/^{238}U$	1σ	$^{238}U/^{232}Th$	$^{207}Pb/^{206}Pb$	$^{206}Pb/^{238}U$
BY-52 (quartz porphyry)									
BY-52-01*	0.04636	0.00110	0.13013	0.00315	0.02017	0.00021	1.42295		129 ± 1
BY-52-02*	0.04795	0.00122	0.13342	0.00338	0.02003	0.00020	2.58939		128 ± 1
BY-52-03*	0.04605	0.00090	0.12823	0.00261	0.02001	0.00017	1.85121		128 ± 1
BY-52-05*	0.05199	0.00111	0.14574	0.00328	0.02015	0.00020	1.38615		129 ± 1
BY-52-06*	0.04715	0.00095	0.13122	0.00267	0.02002	0.00018	2.37868		128 ± 1
BY-52-07*	0.04559	0.00105	0.12629	0.00290	0.01993	0.00019	1.54274		127 ± 1
BY-52-08*	0.04695	0.00118	0.12997	0.00332	0.01995	0.00022	3.24469		127 ± 1
BY-52-12*	0.04804	0.00107	0.13239	0.00283	0.01995	0.00017	4.34137		127 ± 1
BY-52-16*	0.04563	0.00093	0.12616	0.00280	0.01998	0.00018	4.75932		128 ± 1
BY-17-53 (microdiorite)									
BY17-53-01*	0.04872	0.00212	0.13236	0.00569	0.01967	0.00020	8.57519		126 ± 1
BY17-53-02	0.15971	0.00260	10.33234	0.17397	0.46609	0.00432	1.39380	2454 ± 27	
BY17-53-05	0.15858	0.00319	10.37305	0.20066	0.47169	0.00425	1.40449	2440 ± 35	
BY17-53-06	0.13174	0.00279	7.04902	0.14639	0.38520	0.00359	2.15942	2121 ± 37	
BY17-53-08	0.13175	0.00260	7.33762	0.13690	0.40187	0.00338	1.84719	2121 ± 34	
BY17-53-09*	0.04967	0.00294	0.13550	0.00731	0.01970	0.00028	0.93711		126 ± 2
BY17-53-10*	0.04434	0.00417	0.14234	0.01009	0.01975	0.00038	1.46882		126 ± 2
BY17-53-13*	0.05246	0.00263	0.14107	0.00677	0.01967	0.00027	1.05270		126 ± 2
BY17-53-14	0.04872	0.00192	0.21500	0.00863	0.03187	0.00034	0.66594		202 ± 2
BY17-53-15	0.04849	0.00169	0.22076	0.00731	0.03312	0.00037	2.37489		210 ± 2
BY17-53-17*	0.05039	0.00194	0.13849	0.00551	0.01983	0.00020	31.06383		127 ± 1
BY17-53-18*	0.05188	0.00464	0.14094	0.01177	0.01955	0.00036	1.29636		125 ± 2
BY17-53-19*	0.05064	0.00249	0.13649	0.00697	0.01952	0.00031	10.61686		125 ± 2
BY17-53-20*	0.05016	0.00313	0.13612	0.00882	0.01959	0.00026	7.84168		125 ± 2
BY17-53-21*	0.05616	0.00483	0.14991	0.01249	0.01947	0.00041	2.79143		124 ± 3
BY17-53-27	0.13370	0.00230	6.82254	0.11720	0.36865	0.00244	1.17185	2147 ± 30	
BY17-53-31	0.13945	0.00308	7.43108	0.15968	0.38408	0.00313	1.85330	2221 ± 38	
BY17-53-32	0.04927	0.00256	0.23310	0.01236	0.03410	0.00045	1.42675		216 ± 3
BY17-53-33	0.05113	0.00242	0.24583	0.01111	0.03510	0.00045	1.00205		222 ± 3
BY17-53-34	0.05085	0.00171	0.23820	0.00760	0.03399	0.00033	1.94268		215 ± 2
BY17-53-37*	0.04220	0.00303	0.12517	0.00759	0.01932	0.00032	1.29804		123 ± 2
BY17-53-39*	0.04852	0.00387	0.14889	0.00990	0.02019	0.00033	5.72140		129 ± 2
BY17-53-41*	0.04698	0.00251	0.12933	0.00637	0.01970	0.00025	10.64701		126 ± 2

*Data are used to form coherent groups

ore-forming temperature. The minimum trapping temperatures estimated from the inclusions were 230–290 °C for stage 1 and 200–260 °C for stage 2 assemblages.

The trapping pressure conditions can be estimated by the trapping temperatures (Wang et al. 2015c; Chai et al. 2016; Lambert-Smith et al. 2016). We performed calculations in the H_2O–CO_2–NaCl systems and calculated using the FLINCOR software package (Brown 1989). The homogenization temperatures were used to substitute for trapping temperatures calculated for minimum trapping pressures. Stage 1 inclusions yield minimum trapping pressures of 58–139 MPa. The minimum trapping pressures during stage 2 were constrained to 24–68 MPa.

Source of ore fluids

The H–O isotope compositions of quartz from stage 1 are close to the primary magmatic water (Taylor 1974) (Fig. 12). This implies that ore fluid may be dominant by a magmatic fluid at the Baiyun deposit. The quartz samples from stage 3 plot away from the primary magmatic water field (Fig. 12). δD values of quartz samples from stage 3 are lighter and are

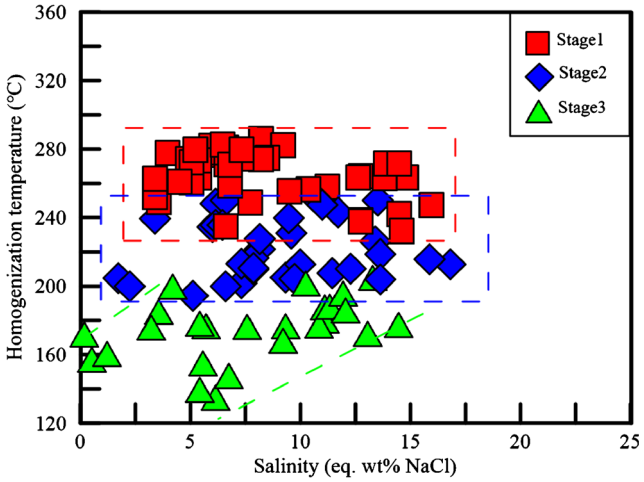

Fig. 11 Temperature versus salinity plot of fluid inclusions showing fluid evolution at the Baiyun deposit

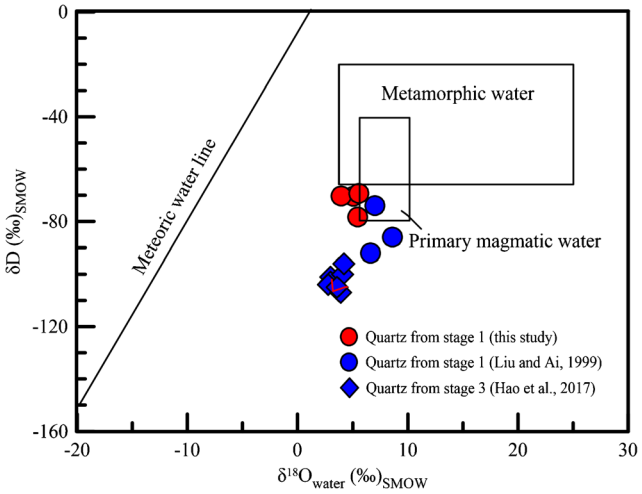

Fig. 12 Isotopic composition of oxygen and hydrogen at the Baiyun deposit. The isotopic fields for common geological waters are from Taylor 1974

depleted up to 20–30‰. Such a shift of δD values might reflect that (1) ore fluids reacted with δD-depleted organic matter (Polya et al. 2000) or (2) ore fluids mixed with low δD meteoric water (Jia et al. 2001). Hypothesis 1 can explain such a variation in hydrogen composition, but there is no organic-rich sediments reported in this orefield. Hypothesis 2 may be a more plausible explanation, because fluid inclusion studies show the characteristics that ore fluids mixed with meteoric water during stage 3.

According to Wang et al. 2015b the calculated $\delta^{18}O_{water}$ and δD values of ore fluids for the Xiaotongjiapuzi gold deposit range between 4 and 9‰ and − 89 to − 92 ‰, respectively. These values are consistent with those of ore fluids for the Baiyun deposit and indicate a magmatic source. Therefore, gold mineralization related to magmatic water may be common in the Qingchengzi orefield.

Constraints on the timing and geodynamic mechanisms of gold mineralization in Liaodong

The pre-ore porphyry and post-ore microdiorite yield weighted mean $^{206}Pb/^{238}U$ ages of 127.8 ± 0.8 Ma and 125.6 ± 1.3 Ma, respectively, indicating that the Baiyun gold deposit formed at ~ 126 Ma. Combining with the fluid inclusion study, we conclude that the Baiyun gold deposit is an intrusion-related vein gold deposit related to the Early Cretaceous magmatism. Wei et al. (2003) dated gold mineralization in the Wulong deposit of the Liaodong gold province at 120 Ma using Rb–Sr dating of pyrite in Au-bearing quartz veins. This result is consistent with a 125–121 Ma zircon SHRIMP U–Pb age of the host granitoids and a monzonitic dike that cuts through the orebodies (Wu et al. 2005a). These ages are similar to the age of gold mineralization in the Baiyun deposit. Therefore, there is a Cretaceous (126–120 Ma) gold mineralization in the Liaodong gold province, similar to that of the Jiaodong gold province.

Wu et al. (2005a) proposed that magmatic activity on the Liaodong Peninsula at 131–117 Ma was associated with extension of the Liaodong gold province and breakup of the NCC in the Early Cretaceous (Yang et al. 2008; Wu et al. 2014). This extension, thinning, and breakup of the lithospheric root likely resulted from subduction of the Pacific plate beneath the NCC (Zhu et al. 2012; Wu et al. 2014). In the Liaodong gold province, gold mineralization (126–120 Ma) was coeval with Early Cretaceous magmatism (131–117 Ma), suggesting that mineralization was related to the breakup of the NCC in the Late Mesozoic.

Dehydration of the subducted Pacific plate led to continuous enrichment in chalcophile elements (Cu, Au, Ag, and Te) of mantle beneath the NCC in the Late Mesozoic (Zhu et al. 2015). When the lithospheric root thinning and breakup, partial melting of enriched mantle would have produced voluminous hydrous, Au- and S-bearing basaltic magma. The mantle-derived magma ascended and served as an important source for ore fluids. Auriferous magmatic fluids would migrate along faults for a long-distance, precipitate ore materials in shallow depth.

Conclusions

(1) The initial ore fluid at the Baiyun gold deposit was moderate salinities, reduced fluid with a moderate temperature. The ore fluid evolved to lower temperature and salinity due to mixing processes. Fluid mixing with meteoric water might result in the precipitation of gold and hessite.

(2) H–O isotope compositions of quartz in stage 1 suggest that the ore fluids were magmatic hydrothermal fluids.
(3) Zircon U–Pb ages of dikes associated with orebodies indicate that gold mineralization occurred at ~ 126 Ma. The Baiyun gold deposit is an intrusion-related vein gold deposit that formed during continental extension triggered by the breakup of the NCC in the Early Cretaceous.

Acknowledgments We would like to thank Fluid Inclusion Laboratories, the China University of Geosciences (Beijing), the Institute of Geology and Geophysics at the Chinese Academy of Sciences (IGGCAS), and Sample Solution Analytical Technology Corporation for their analytical work. We acknowledge the Editor-in-Chief Abdullah M. Al-Amri and the highly constructive comments of anonymous reviewers.

Funding information This study was supported by the National Key R & D Program of China (Grant No. 2016YFC0600108), State Key Laboratory of Lithospheric Evolution (S201605), and National Key R & D Program of China (Grant No. 2016YFC0600101).

References

Anderson MR, Rankin AH, Spiro B (1992) Fluid mixing in the generation of mesothermal gold mineralisation in the Transvaal Sequence, Transvaal, South Africa. Eur J Mineral 4:933–948

Arehart GB (1996) Characteristics and origin of sediment-hosted disseminated gold deposits: a review. Ore Geol Rev 11:383–403

Bowers TS, Helgeson HC (1983) Calculation of the thermodynamic and geochemical consequences of nonideal mixing in the system H_2O-CO_2-NaCl on phase relations in geologic systems: equation of state for H2O-CO2-NaCl fluids at high pressures and temperatures. Geochim Cosmochim Acta 47:1247–1275

Brown PE (1989) FLINCOR; a microcomputer program for the reduction and investigation of fluid-inclusion data. Am Mineral 74:1390–1393

Brown PE, Lamb WM (1989) P-V-T properties of fluids in the system $H_2O \pm CO_2 \pm$ NaCl: new graphical presentations and implications for fluid inclusion studies. Geochim Cosmochim Acta 53:1209–1221

Cao MJ, Qin KZ, Li GM, Evans NJ, Jin LY (2014) Abiogenic Fischer–Tropsch synthesis of methane at the Baogutu reduced porphyry copper deposit, western Junggar, NW-China. Geochim Cosmochim Acta 141:179–198

Chai P, Sun JG, Xing SW et al (2016) Ore geology, fluid inclusion and $^{40}Ar/^{39}Ar$ geochronology constraints on the genesis of the Yingchengzi gold deposit, southern Heilongjiang Province, NE China. Ore Geol Rev 72(Part 1):1022–1036

Clayton RN, O'Neil JR, Mayeda TK (1972) Oxygen isotope exchange between quartz and water. J Geophys Res 77:3057–3067

Cline JS, Hofstra AA (2000) Ore-fluid evolution at the Getchell Carlin-type gold deposit, Nevada, USA. Eur J Mineral 12:195–212

Diamond LW (2001) Review of the systematics of CO2–H2O fluid inclusions. Lithos 55:69–99

Duan XX, Zeng QD, Yang JH, Liu J, Wang Y, Zhou L (2014) Geochronology, geochemistry and Hf isotope of Late Triassic magmatic rocks of Qingchengzi district in Liaodong peninsula, Northeast China. J Asian Earth Sci 91:107–124

Duan XX, Zeng QD, Wang YB, Zhou LL, Chen B (2017) Genesis of the Pb−Zn deposits of the Qingchengzi ore field, eastern Liaoning, China: constraints from carbonate LA−ICPMS trace element analysis and C–O–S–Pb isotopes. Ore Geol Rev 89:752–771

Fan HR, Zhai MG, Xie YH, Yang JH (2003) Ore-forming fluids associated with granite-hosted gold mineralization at the Sanshandao deposit, Jiaodong gold province, China. Mineral Deposita 38:739–750

Groves DI, Santosh M (2016) The giant Jiaodong gold province: the key to a unified model for orogenic gold deposits? Geosci Front 7:409–417

Hall DL, Sterner SM, Bodnar RJ (1988) Freezing point depression of NaCl-KCl-H_2O solutions. Econ Geol 83:197–202

Hao LB, Zhao X, Zhao YY (2017) Stable isotope characteristics and ore genesis of the Baiyun gold deposit, Liaoning province. J Jilin Univ (Earth Sci Ed) 47:442–451 (in Chinese with English abstract)

Hayashi K, Ohmoto H (1991) Solubility of gold in NaCl-and H_2S-bearing aqueous solutions at 250–350°C. Geochim Cosmochim Acta 55:2111–2126

Hedenquist JW, Henley RW (1985) The importance of CO_2 on freezing point measurements of fluid inclusions; evidence from active geothermal systems and implications for epithermal ore deposition. Econ Geol 80:1379–1406

Hofstra AH, Leventhal JS, Northrop HR, Landis GP, Rye RO, Birak DJ, Dahl AR (1991) Genesis of sediment-hosted disseminated-gold deposits by fluid mixing and sulfidization: chemical-reaction-path modeling of ore-depositional processes documented in the Jerritt Canyon district, Nevada. Geology 19:36–40

Hu GY, Li YH, Fan CF, Hou K, Zhao Y, Zeng L (2015) In situ LA–MC–ICP–MS boron isotope and zircon U–Pb age determinations of Paleoproterozoic borate deposits in Liaoning Province, northeastern China. Ore Geol Rev 65:1127–1141

Jia Y, Li X, Kerrich R (2001) Stable isotope (O, H, S, C, and N) systematics of quartz vein systems in the turbidite-hosted Central and North Deborah Gold deposits of the Bendigo Gold Field, Central Victoria, Australia: constraints on the origin of ore-forming fluids. Econ Geol 96:705–721

Lambert-Smith JS, Lawrence DM, Vargas CA, Boyce AJ, Treloar PJ, Herbert S (2016) The Gounkoto Au deposit, West Africa: constraints on ore genesis and volatile sources from petrological, fluid inclusion and stable isotope data. Ore Geol Rev 78:606–622

Lécuyer C, Dubois M, Marignac C, Gruau G, Fouquet Y, Ramboz C (1999) Phase separation and fluid mixing in subseafloor back arc hydrothermal systems: a microthermometric and oxygen isotope study of fluid inclusions in the barite-sulfide chimneys of the Lau Basin. J Geophys Res Sol Earth 104:17911–17927

Li XC, Fan HR, Santosh M, Hu FF, Yang KF, Lan TG (2013) Hydrothermal alteration associated with Mesozoic granite-hosted gold mineralization at the Sanshandao deposit, Jiaodong Gold Province, China. Ore Geol Rev 53:403–421

Liu GP, Ai YF (1999) A discussion on some major problems of the Baiyun gold deposit, eastern Liaoning. Mineral Deposits 18:219–225 (in Chinese with English abstract)

Liu GP, Ai YF (2000) Studies on the mineralization age of Baiyun gold deposit in Liaoning. Acta Petrol Sin 16:627–632 (in Chinese with English abstract)

Liu DY, Nutman AP, Compston W, Wu JS, Shen QH (1992) Remnants of ≥3800 Ma crust in the Chinese part of the Sino-Korean craton. Geology 20:339–342

Liu DY, Wilde SA, Wan YS, Wu J, Zhou H, Dong C, Yin X (2008) New U-Pb and Hf isotopic data confirm Anshan as the oldest preserved segment of the North China Craton. Am J Sci 308:200–231

Liu YS, Gao S, Hu ZC, Gao C, Zong K, Wang D (2010) Continental and oceanic crust recycling-induced melt–peridotite interactions in the trans-North China Orogen: U–Pb dating, Hf isotopes and trace elements in zircons from mantle xenoliths. J Petrol 51:537–571

Liu KH, Liu FX, Su JF et al (2012a) Geological features and genesis of Huangdianzi gold deposit in Fengcheng City, Liaoning Province. Jilin Geol 31:35–40 (in Chinese with English abstract)

Liu SW, Zhang J, Li QG et al (2012b) Geochemistry and U–Pb zircon ages of metamorphic volcanic rocks of the Paleoproterozoic Lüliang complex and constraints on the evolution of the Trans-North China Orogen, North China craton. Precambrian Res 222–223:173–190

Lu XP, Wu FY, Guo JH, Wilde SA, Yang JH, Liu XM, Zhang XO (2006) Zircon U–Pb geochronological constraints on the Paleoproterozoic crustal evolution of the Eastern block in the North China craton. Precambrian Res 146:138–164

Ludwig KR (2003) ISOPLOT 3.0: a geochronological toolkit for Microsoft Excel. Berkeley Geochronol Cent Spec Publ 4:74

Luo Y, Sun M, Zhao GC, Li S, Xu P, Ye K, Xia X (2004) LA-ICP-MS U–Pb zircon ages of the Liaohe Group in the Eastern Block of the North China Craton: constraints on the evolution of the Jiao-Liao-Ji Belt. Precambrian Res 134:349–371

Luo Y, Sun M, Zhao GC, Li S, Ayers JC, Xia X, Zhang J (2008) A comparison of U–Pb and Hf isotopic compositions of detrital zircons from the North and South Liaohe Groups: constraints on the evolution of the Jiao-Liao-Ji Belt, North China Craton. Precambrian Res 163:279–306

Meng E, Liu FL, Liu PH, Liu CH, Yang H, Wang F, Shi JR, Cai J (2014) Petrogenesis and tectonic significance of Paleoproterozoic metamafic rocks from central Liaodong Peninsula, Northeast China: evidence from zircon U–Pb dating and in situ Lu–Hf isotopes, and whole-rock geochemistry. Precambrian Res 247:92–109

Mikucki EJ (1998) Hydrothermal transport and depositional processes in Archean lode-gold systems: a review. Ore Geol Rev 13:307–321

Neyedley K, Hanley JJ, Fayek M, Kontak DJ (2017) Textural, fluid inclusion, and stable oxygen isotope constraints on vein formation and gold precipitation at the 007 deposit, Rice Lake Greenstone Belt, Bissett, Manitoba, Canada. Econ Geol 112:629–660

Polya DA, Foxford KA, Stuart F, Boyce A, Fallick AE (2000) Evolution and paragenetic context of low δD hydrothermal fluids from the Panasqueira W-Sn deposit, Portugal: new evidence from microthermometric, stable isotope, noble gas and halogen analyses of primary fluid inclusions. Geochim Cosmochim Acta 64:3357–3371

Roedder E (1984) Fluid inclusions. Rev Mineral 12:1–664

Seward TM (1973) Thio complexes of gold and the transport of gold in hydrothermal ore solutions. Geochim Cosmochim Acta 37:379–399

Song B, Nutman AP, Liu DY, Wu JS (1996) 3800 to 2500 Ma crustal evolution in the Anshan area of Liaoning Province, northeastern China. Precambrian Res 78:79–94

Taylor HP (1974) The application of oxygen and hydrogen isotope studies to problems of hydrothermal alteration and ore deposition. Econ Geol 69:843–883

Tombros S, Seymour KS, Williams-Jones AE, Spry PG (2007) The genesis of epithermal Au-Ag-Te mineralization, Panormos Bay, Tinos Island, Cyclades, Greece. Econ Geol 102:1269–1294

Wan YS, Song B, Liu DY, Wilde SA, Wu J, Shi Y, Yin X, Zhou H (2006) SHRIMP U–Pb zircon geochronology of Palaeoproterozoic metasedimentary rocks in the North China Craton: evidence for a major Late Palaeoproterozoic tectonothermal event. Precambrian Res 149:249–271

Wang YF, Li XH, Jin W, Zhang JH (2015a) Eoarchean ultra-depleted mantle domains inferred from ca. 3.81Ga Anshan trondhjemitic gneisses, North China craton. Precambrian Res 263:88–107

Wang YC, Wang KY, Zhang M et al (2015b) Characteristics of hydrothermal superimposition mineralization and fluid origins of the Xiaotongjiapuzi Gold Deposit in Liaoning Province. Geol Explor 51:79–87 (in Chinese with English abstract)

Wang ZL, Yang LQ, Guo LN et al (2015c) Fluid immiscibility and gold deposition in the Xincheng deposit, Jiaodong Peninsula, China: a fluid inclusion study. Ore Geol Rev 65(Part 3):701–717

Wang XP, Peng P, Wang C, Yang SY (2016) Petrogenesis of the 2115Ma Haicheng mafic sills from the Eastern North China craton: implications for an intra-continental rifting. Gondwana Res 39:347–364

Wang XP, Peng P, Wang C, Yang S, Söderlund U, Su X (2017) Nature of three episodes of Paleoproterozoic magmatism (2180Ma, 2115Ma and 1890Ma) in the Liaoji belt, North China with implications for tectonic evolution. Precambrian Res 298:252–267

Wei JH, Liu CQ, Tang HF (2003) Rb-Sr and U-Pb isotopic systematics of pyrite and granite in Liaodong gold province, North China: implication for the age and genesis of a gold deposit. Geochem J 37:567–577

Wilde AR, Layer P, Mernagh T, Foster J (2001) The Giant Muruntau gold deposit: geologic, geochronologic, and fluid inclusion constraints on ore genesis. Econ Geol 96:633–644

Wu FY, Lin JQ, Wilde SA et al (2005a) Nature and significance of the Early Cretaceous giant igneous event in eastern China. Earth Planet Sci Lett 233:103–119

Wu FY, Yang JH, Wilde SA, Zhang XO (2005b) Geochronology, petrogenesis and tectonic implications of Jurassic granites in the Liaodong Peninsula, NE China. Chem Geol 221:127–156

Wu FY, Xu YG, Zhu RX, Zhang GW (2014) Thinning and destruction of the cratonic lithosphere: a global perspective. Sci China Earth Sci 57:2878–2890

Xie LW, Yang JH, Wu FY, Yang YH, Wilde SA (2011) PbSL dating of garnet and staurolite: constraints on the Paleoproterozoic crustal evolution of the Eastern Block, North China Craton. J Asian Earth Sci 42:142–154

Yang JH, Wu FY, Wilde SA, Belousova E, Griffin WL (2008) Mesozoic decratonization of the North China block. Geology 36:467–470

Yang LQ, Deng J, Guo L-N, Wang ZL, Li XZ, Li JL (2016) Origin and evolution of ore fluid, and gold-deposition processes at the giant Taishang gold deposit, Jiaodong Peninsula, eastern China. Ore Geol Rev 72:585–602

Yu G, Chen JF, Xue CJ, Chen Y, Chen F, du X (2009) Geochronological framework and Pb, Sr isotope geochemistry of the Qingchengzi Pb–Zn–Ag–Au orefield, Northeastern China. Ore Geol Rev 35:367–382

Zezin DY, Migdisov AA, Williams-Jones AE (2007) The solubility of gold in hydrogen sulfide gas: an experimental study. Geochim Cosmochim Acta 71:3070–3081

Zhang X, Cawood PA, Wilde SA et al (2003) Geology and timing of mineralization at the Cangshang gold deposit, north-western Jiaodong Peninsula, China. Mineral Deposita 38:141–153

Zhang P, Li B, Li J et al (2016) Re-Os isotopic dating and its geological implication of gold bearing pyrite from the Baiyun gold deposit in Liaodong rift. Geotecton Metallog 40:731–738 (in Chinese with English abstract)

Zhou GC (2017) Studies on the genesis of Baiyun gold deposit in Liaodong (Master). Kunming University of Science and Technology. (in Chinese with English abstract)

Zhu RX, Xu YG, Zhu G, Zhang HF, Xia QK, Zheng TY (2012) Destruction of the North China Craton. Sci China Earth Sci 55:1565–1587

Zhu RX, Fan HR, Li JW, Meng QR, Li SR, Zeng QD (2015) Decratonic gold deposits. Sci China Earth Sci 58:1523–1537